



Rock Adaptability of TBM Variable Cross-section Cutter Ring Based on Finite Element Simulation

Jia-Li Zhao¹ · Xian-Yong Zhu¹ · Cheng Jiang¹ · Song Yang¹ · Xiong Xiao¹

Received: 2 August 2022 / Accepted: 18 January 2023 / Published online: 6 February 2023
© The Author(s), under exclusive licence to Springer-Verlag GmbH Austria, part of Springer Nature 2023

Abstract

A cutter ring is a consumable tool used by a tunnel boring machine (TBM) to break rock, affecting the cost and time limit of tunnel engineering. In this paper, based on the working principle of the cutter ring, the failure form of cutter rings, and the mechanical properties of rock, a variable cross-section (VCS) cutter ring is optimized based on the existing constant cross-section (CCS) cutter ring. The finite element method was used to model the Beishan granite, and the mechanical properties of the granite were simulated. The average discrepancy rate of the four key parameters was 1.19% compared with the experimental results. The linear rock cutting experiment of the disc cutter in Beijing University of Technology was simulated, the simulation results of normal force are similar to the reality. The digital models of the 20-in CCS cutter ring and 30 types of VCS cutter rings are established, and modal, impact response, and cutting rock simulations are conducted. The results demonstrate that the natural frequencies of the two types of cutter rings are very close to 6.72 rad/s, confirming the feasibility of interchange. The impact resistance of most of the 30 VCS rings is higher than that of CCS rings, and the rock-breaking effect of all VCS rings outperforms that of the CCS rings. The VCS ring with the highest crushing adaptability of the rock model in this simulation experiment was obtained by statistical analysis of 3D data. This experimental method of rock adaptability can obtain the optimal design parameters of VCS cutter rings for a particular rock model. VCS cutter rings have the potential to support establishing a tool selection system with rock adaptability based on extensive experimental data in the future.

Highlights

- According to the working principle, failure mode of TBM disk cutter and rock characteristics, a variable cross-section (VCS) diskcutter is designed.
- The simulation model of linear rock cutting is established according to the real experiment, and the validity of the simulation model is verified.
- The impact resistance and damaged rock performance of 30 kinds of VCS cutter rings were ranked using a statistical analysis method with 3D data.

Keywords Disc cutter · Cutter ring · Variable cross-section · Simulation · Rock breaking · Rock adaptability

✉ Xian-Yong Zhu
zhuxy@jlu.edu.cn

✉ Cheng Jiang
jiangcheng@jlu.edu.cn

¹ School of Mechanical and Aerospace Engineering,
Jilin University, Nanguan 5988 Renmin Street,
Changchun 130022, Jilin, China

1 Introduction

The tool system is integral to the tunnel boring machine (TBM). Its performance is directly related to TBM tunneling efficiency and reliability (Herrenknecht et al. 2008). The ring of the disc cutter is the part that directly contacts the rock, so the cutter ring is critical to breaking the rock (Liu et al. 2016a, b). After years of development, the disc cutter's size and blade section shape have changed significantly. The size change is reflected primarily in the external diameter size of

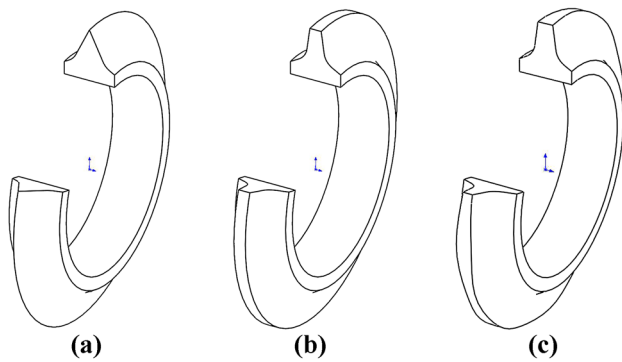


Fig. 1 Schematic of cutter ring section type: **a** wedge, **b** CCS, and **c** VCS

the disc cutter increasing from 11 to 20 in, and the bearing capacity has also increased from the original 85 to 312 kN. The increase in the size of the ring can increase the allowable wear thickness, increasing service life and decreasing tool change time. However, when the outer diameter of the disc cutter increases, its overall weight increases significantly, requiring a much higher bearing capacity. Therefore, the cutter diameters commonly used in TBM projects are 17, 19, and 20 in (Huo et al. 2011).

The blade section shape has evolved from a wedge section to a constant cross-section (CCS). Some scholars have recently proposed the variable cross-section (VCS) ring, as depicted in Fig. 1. The blade width of the ring with wedge section increases significantly after wear, resulting in a sharp increase in cutter load. It also causes a sharp increase in the moving resistance of the cutter head (Balci et al. 2012). The VCS ring is improved based on the CCS ring so that the contact width between the blade and rock changes periodically, which is theoretically conducive to rock cracking and crushing. However, few relevant research results exist (Zhao et al. 2022).

Based on the statistics of several TBM engineering cases, the cost of disc cutter loss accounts for one-fourth to one-fifth of the TBM construction cost, even as high as one-third in some extreme cases (Wang et al. 2012; Geng et al. 2017). The total downtime, tool checking, and tool replacement time caused by cutter failure are more than one-third of the TBM construction time (Liu et al. 2017). The rock fragmentation energy of the disc cutter is directly related to TBM tunneling efficiency and cost (Gong et al. 2016).

With the continuous development of TBM technology, more scholars have proposed a physical experiment method of the disc cutter destroying rock in a laboratory to explore its rock-breaking ability (Qi et al. 2016; Liu et al. 2016a, 2016b). Each of these methods has advantages and disadvantages. The full-scale linear cutting machine (LCM) experiment has been widely accepted as the most accurate and reliable test method because of its weak size and boundary

effects (Chang et al. 2006; Cardu et al., 2017; Park et al. 2018; Pan et al. 2018).

Xia et al. (2017) conducted a rock-breaking simulation of a cutter under a free surface condition using AUTODYN and obtained the variation rule of cutter load response. Yang et al. (2015) used LS-DYNA to establish a disc-cutter rotary rock-breaking simulation model based on the brittle fracture rock model. They studied the internal stress distribution of rock mass under the action of the cutter and the variation rule of load under different cutter wear degrees. Xiao et al. (2017) studied the dynamic change law of the cutter's rock-breaking load by defining a new rock material constitutive method and the FEM smoothed particle hydrodynamics (SPH) coupling method in ABAQUS. Moon et al. (2011) used the discrete element method (DEM) particle flow code (PFC) to establish a simulation model of cutter rock-breaking under different cutter structural and geological parameters. They studied the load response law and rock-breaking energy consumption change law under different working conditions. Choi et al. (2014) used the numerical analysis method of disc cutter rock-breaking based on particle flow software.

Disc cutter ring performance is the crucial factor affecting the cost and duration of tunnel construction, so it is necessary to conduct in-depth research on it. Studying the cutter ring performance from the aspect of section shape optimization is a relevant research direction. However, with the widespread application of CCS cutter rings, the relevant research is less and less, but this does not mean the end. Because of the complexity of geological conditions, the production efficiency of TBM tunnel engineering can be improved using cutters with higher adaptability. Establishing a tool selection system with a minimum level of rock adaptability will further promote the development of TBM technology.

This paper introduces a VCS cutter ring design process that can adapt to a particular type of rock, including the parametric design of a VCS cutter ring digital model. A FEM experiment model was established and, its validity was verified. A modal simulation was used to verify the feasibility of exchanging VCS cutter rings with CCS cutter rings to compare the impact resistance of a VCS cutter with different parameters. For each type of granite, different VCS cutter rings were used for rolling simulation and comparison. Finally, the optimal parameters of the VCS cutter ring are summarized and counted.

2 Modeling Design of Cutter Ring

2.1 Principle of Rock Breakage

A disc cutter is an assembly with an independent mechanical structure, as depicted in Fig. 2. The cutter ring can rotate

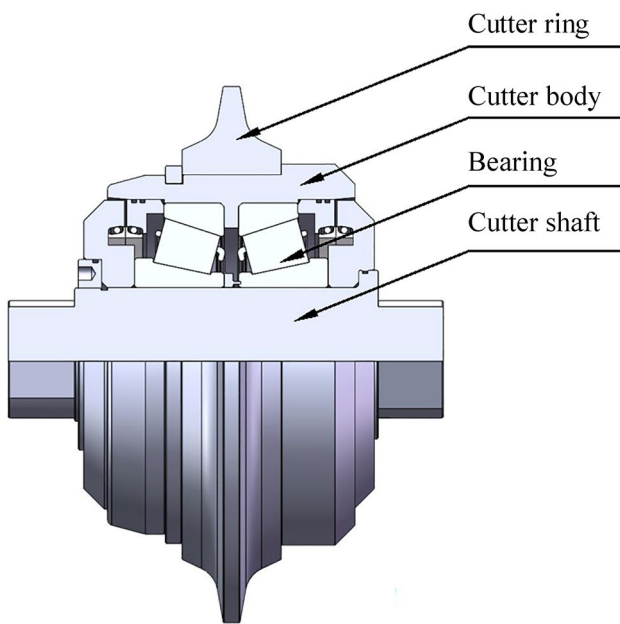


Fig. 2 Disc cutter assembly

along the tool shaft with the tool body under torsion force generated by external friction. During TBM excavation, the hydraulic cylinder pushes the spindle and tool system along the axis while the spindle drives the tool to rotate. The disc cutter first touches the rock on the cutter head and then gradually penetrates the shallow depth of the rock for rolling.

The rock is subjected to impact, extrusion, tensile, shear, vibration, and other forms of force from the disc cutter, and cracks are gradually generated internally and extended around. When cracks are connected with cracks

or free surfaces, broken fragments are formed, as depicted in Fig. 3. The disc cutter rotates with the spindle of the cutter head and rotates with the cutter axis because of the friction of the rock. Therefore, the relative motion between the disc cutter and rock mass integrates two forms of penetration and rolling (Rostami et al., 2013; Geng et al. 2016; Xia et al. 2018).

Wang et al. (2017) described the mathematical model used to describe rock destructive power studied by scholars. The most widely cited is the Colorado School of Mines (CSM) mathematical model developed by The CSM (Gertsch et al. 2007) as early as 1993. This mathematical model is based on the full-size LCM experimental database and has been confirmed reliable by many previous experiments. It has long been instrumental in studying destructive rock forces. In the CSM model, the pressure distribution in the crushing zone is calculated by Eq. (1), for which all variables are depicted in Fig. 4.

$$P(\theta) = P_0 \left(\frac{\varphi}{\theta} \right)^\psi \tag{1}$$

where ψ is the constant of the pressure distribution function derived from extensive LCM physical experimental data. For the CCS-type cutter ring, this value is usually set to 0.2, where φ is the contact angle between the rock and the tool, θ is the differential angle, and P_0 is the base pressure established through linear regression analysis of multiple test data, as follows:

$$\varphi = \cos^{-1} \left(\frac{R-p}{R} \right) \tag{2}$$

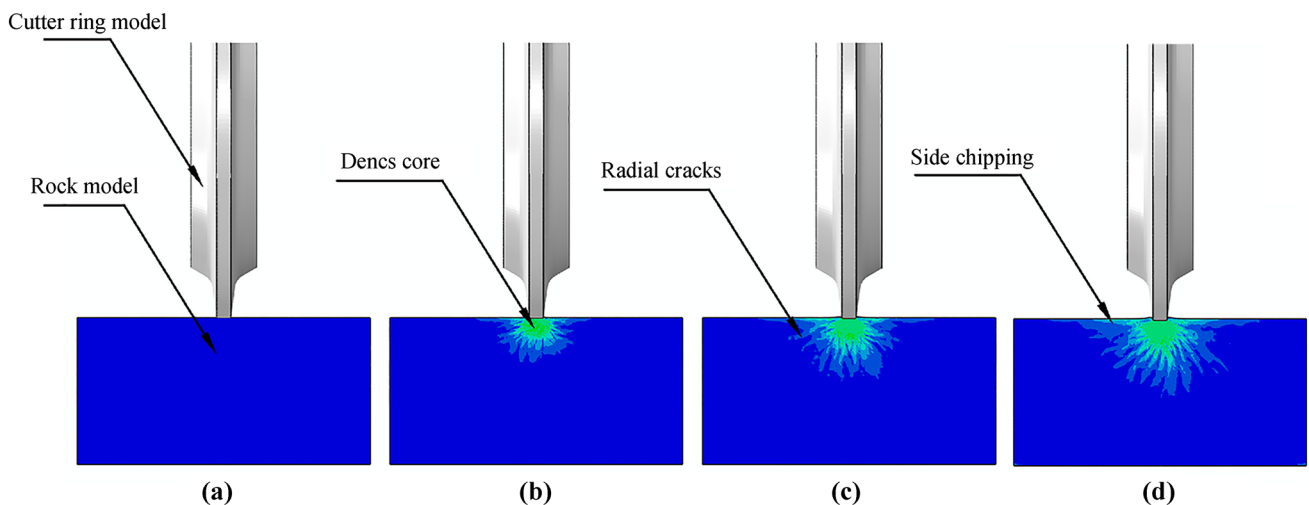


Fig. 3 Schematic of rock stress change during cutting ring penetration: a before contact, b rock compaction stage, c crack propagation stage, and d cracks extending and rock fragments falling off stage

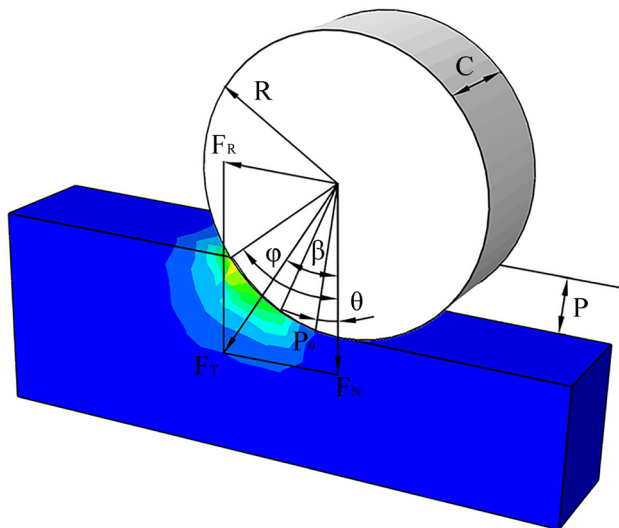


Fig. 4 Mathematical model variables

$$P_0 = C^3 \sqrt{\frac{\sigma_c^2 \sigma_t S}{\varphi \sqrt{RT}}} \tag{3}$$

where R is the unit of cutter radius (m), P is the penetration degree (m), C is the infinite dimension constant (usually $C = 2.12$), σ_c is the uniaxial compressive strength (UCS, in MPa) of rock, σ_t is the tensile strength (MPa), S is the spacing between cutters (m), and C is the width of the blade

(m). By integrating the pressure and area on the contact area, the total cutting force F_T (KN) can be calculated as follows:

$$F_T = \int_0^\varphi TRP(\theta)d(\theta) = \frac{TRP_0\varphi}{1 + \psi} \tag{4}$$

The components of the total cutting force in the penetration and rolling directions are F_N (KN) and F_R (KN), where the direction is perpendicular to the rock surface downward and parallel to the rock surface along the motion track direction. Their ratio, usually called the cutting factor, is described by CC, as follows:

$$CC = \frac{F_R}{F_T} = \tan\beta \tag{5}$$

Assuming that the rock is isotropic material, there are no macroscopic factors such as joints, and the pressure in the contact area is evenly distributed, the size of angle β is half of the contact angle:

$$\beta = \frac{\varphi}{2} \tag{6}$$

Therefore, F_N and F_R can be calculated as follows:

$$F_N = F_T \cos\beta = \frac{TRP_0\varphi}{1 + \psi} \cos\frac{\varphi}{2} \tag{7}$$

$$F_R = F_T \sin\beta = \frac{TRP_0\varphi}{1 + \psi} \sin\frac{\varphi}{2} \tag{8}$$

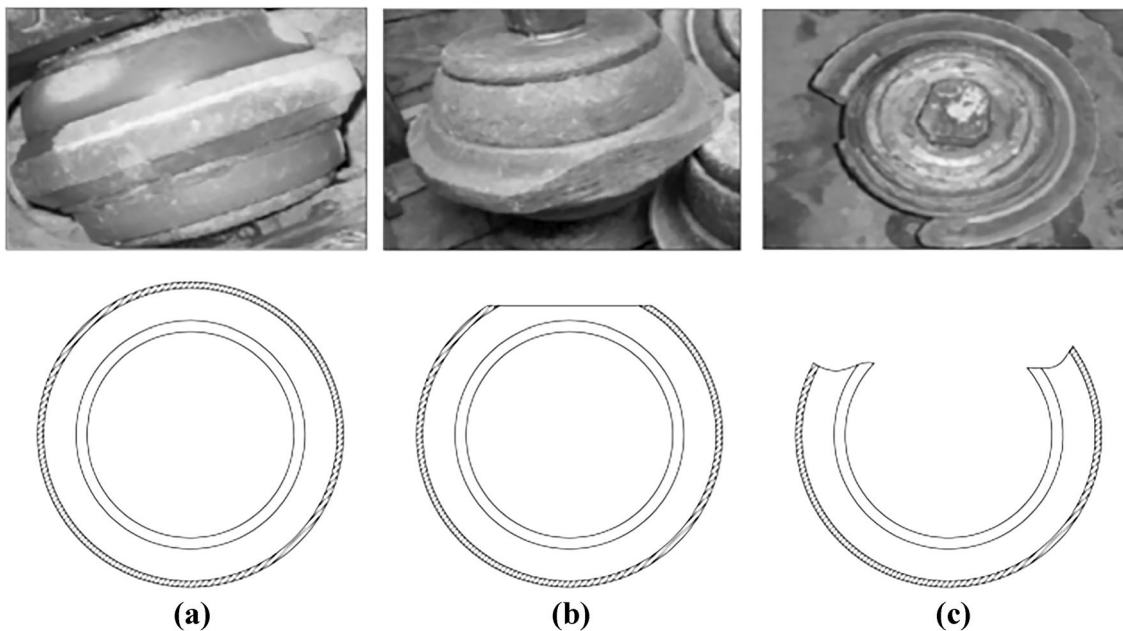


Fig. 5 Schematic of primary cutter ring failure types: **a** normal wear failure, **b** abnormal local wear failure, and **c** abnormal fracture failure

This model has been used to estimate the performance of TBM tool systems in many tunneling projects with high success (Li et al. 2016).

2.2 Failure Modes of the Cutter Ring

A cutter ring is a consumable tool for TBM rock crushing, and its primary failure forms include normal wear, abnormal wear, and fracture. For example, Fig. 5a illustrates normal wear, which occurs at the outer edge of the cutter ring, and the wear depth is typically about 5% of the radius of the cutter ring (Barzegari et al. 2015). Figure 5b, c illustrate abnormal wear. In contrast, Fig. 5b illustrates local wear and change, primarily because the geological condition of rock to cutter ring friction torque cannot demand the rotation of the cutter ring start, and the cutter around the circle cutter center repeatedly stops rotating. When the rolling friction transforms into sliding friction, the friction causes locally-occurring fatigue, increasing wear and tear. Figure 5c illustrates the cutter ring fracture, caused primarily by stress concentration caused by complex geological structure and frequent occurrence of impact and other unstable loads in the working process. The wear failure of the cutter ring is affected by two groups of factors: (1) geological conditions, including complete rock parameters, rock mass parameters, and environmental factors, and (2) TBM operation dynamic parameters, including cutter head speed and thrust.

Many studies have found that the number of abnormal failures of cutter rings accounts for a high proportion of the total failures (Mirahmadi et al. 2017). Hassanpour (2018) introduced statistics on the use of cutter rings in the Ghomrood Water Conveyance Tunnel project in Iran. The results demonstrated that 20% of the total consumption of cutter rings failed abnormally, causing substantial economic losses. Therefore, research on the performance of the cutter ring itself is the only way to address cutter ring failure. Furthermore, improving the adaptability of the cutter ring in complex geological environments is critical to reducing the high proportion of abnormal failure.

2.3 Rock Mechanical Characteristics

The design and application of TBM are based on the study of rock mechanical characteristics, so improving the rock adaptability of the disc cutter is an effective method to improve the working efficiency of TBM (Liu and Cao 2016; Lin et al. 2017). Rock is the most important basic unit of underground rock mass, also known as structure in the geological environment—this structure and joints, fissures, folds, voids, faults, and other structural planes constitute underground rock mass. Therefore, the rock mass faced in tunnel engineering is a highly complex and changeable collection of materials (Plinninger et al. 2003; Gong et al.

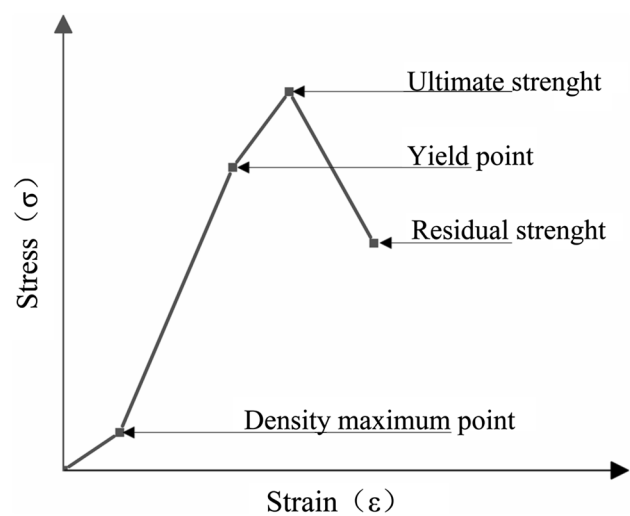


Fig. 6 Typical compressive stress–strain curves of rocks

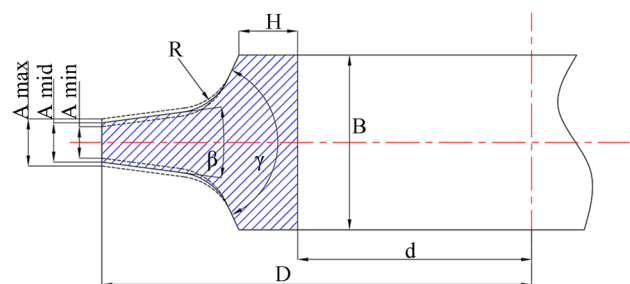


Fig. 7 Schematic of parametric design of cutter ring: **A** width of the blade, **B** thickness of the body, **D** outer diameter, **d** inner diameter, **H** shoulder width, **R** rounded shoulder and blade, (β) blade angle, and (γ) shoulder angle

2006). However, compared with complex rock structures, single and intact rocks are often more stable and challenging to break (Tan et al. 2018).

Therefore, the study of the relationship between the mechanical properties of a single stable rock body and the motion characteristics of the cutter ring is the basis for improving the lithologic breaking energy of the cutter ring (Liu et al. 2015a, b). Rock has brittle material properties with much lower tensile and shear strength than compressive strength. UCS is one of the most commonly used parameters in tool life prediction (Li et al. 2018). The proposed prediction model uses UCS as the input variable and obtains acceptable prediction results. Typical hard-rock stress–strain diagrams are depicted in Fig. 6.

2.4 Parametrization Design

Based on the principles of rock-breaking of the cutter ring, failure mode, and mechanical properties of rock introduced

above, optimization should be conducted based on the cutter ring's geometric shape. The optimization objective is to design a new cutter ring that can replace the cutter ring commonly used in the existing engineering, has a higher rock destructive effect than the previous cutter ring, and adapts to the complex surrounding rock environment.

A parametric design is conducted for the traditional CCS cutter ring, with the variables depicted in Fig. 7. According to the mechanical properties of rock, the tensile strength and shear strength are far less than the compressive strength. If the tensile and shear stress produced by the cutter ring on the rock increases, the destructive effect of the cutter ring on the rock is strengthened. According to the mechanical principle of rock destruction by the cutter ring, the tensile and shear stress produced by the cutter ring on the rock are caused primarily by the edge and the edge side.

Consequently, increasing the contact distance between the blade and the rock by changing the shape of the blade increases the tensile and shear stress generated by the cutter ring on the rock. Based on the failure form of the cutter ring, the abnormal failure of the cutter ring is caused primarily by insufficient friction torque and frequent impact load. Therefore, if the friction between the blade of the cutter ring and the rock is improved and the impact resistance of the cutter ring is enhanced, some abnormal failures may be avoided.

Assuming that the cutter ring rolls along a straight line, the marks left by the CCS cutter ring rolling over the rock surface should be rectangular, as represented by the solid black line in Fig. 8a. The stress distribution trajectory left by the cutter ringside on the rock surface should be in the arrow direction, as depicted in Fig. 8a. Under the guaranteed condition of invariable contact area, changes occur to the upper and lower edges of a rectangular curve, as represented by the black outline curve in Fig. 8b. In that case, the cutter circle track has a lateral stress distribution in the rock surface, as depicted in Fig. 8b in the direction of the arrow, increasing the length of the effect on the rock and improving

the cutter laps on the rock's side work. The work performed by the blade to the rock shear also increases, and the increase in work increases the energy transferred to the rock by the blade rim, strengthening the destructive effect.

Furthermore, the cutter ring is repeatedly rolled on the same path during operation. The track left by the CCS cutter ring is depicted in Fig. 8c, while the track left by the VCS cutter ring is depicted in Fig. 8d. The difference in damage range between the two types of cutter rings is evident. The frictional resistance of the VCS ring is conceivably higher than that of the CCS ring, which improves the torque of the ring rotation and reduces the probability of local wear failure caused by insufficient friction.

Achieving these objectives requires adjusting two design parameters of the cutter ring. The first is the section characteristics of the blade ring, reflected primarily in the three-blade-width design. As depicted in Fig. 7, A_{max} is the maximum blade width, A_{mid} is the middle blade width (equal to the corresponding blade width of the CCS ring), and A_{min} is the minimum blade width. The sections composed of these three

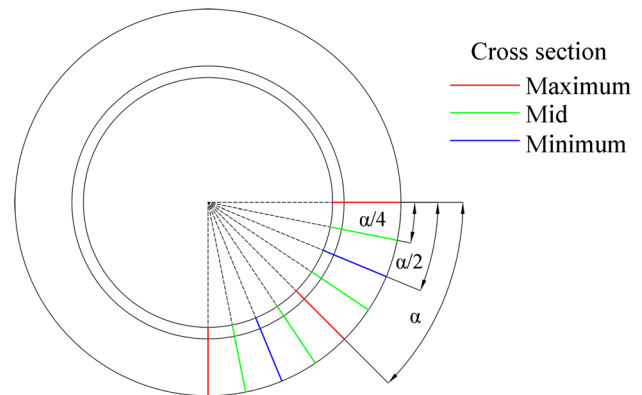


Fig. 9 Design diagram of number of blade changes of VCS cutter ring: (α) angle corresponding to each change in blade shape

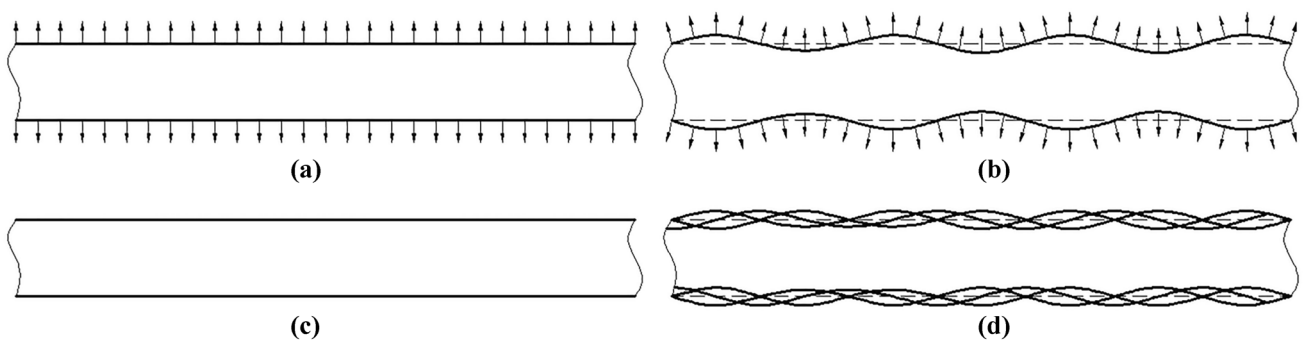


Fig. 8 Sketch diagram of rock rolling by cutter rings: **a** single rolling track and lateral stress distribution of CCS cutter ring, **b** single rolling track and lateral stress distribution of VCS cutter ring, **c** track of CCS

cutter ring rolling several times overlaps, and **d** track of a VCS cutter ring rolling several times overlaps

blade widths are the *maximum*, *middle*, and *minimum* sections. Definition A is the variation range of the cutter ring curve trajectory, calculated as follows:

$$A = \frac{A_{max} + A_{min}}{2} \tag{9}$$

The second is the variation characteristics of the section of the cutter ring, reflected primarily in the number of curve marks generated by each rolling circle of the cutter ring—the number of blade width changes, defined as *T*. Furthermore, the circumference angle α corresponding to each complete curve length must be defined, as depicted in Fig. 9. Considering the influence of the dynamic balance of the cutter ring and the natural frequency, the value range of *T* should satisfy the following conditions:

$$T = \frac{360^\circ}{\alpha} (T \in N, T > 1) \tag{10}$$

Given the influence of changes to the cutter blade shape circle on shock resistance, it is necessary to analyze the

cutter circle of the shock response. Because the thickness of the outer edge of the CCS cutter ring is the same, the stress distribution of the response is uniformly expanded when any position on the outer edge is subjected to the same impact load. However, because the thickness of the outer edge of the VCS cutter ring changes continuously, the stress distribution is not uniform when any position on the outer edge of the VCS is subjected to the same impact load, as depicted in Fig. 10.

Several cutter ring models were established for simulation, and the 20-in CCS cutter ring common in engineering was used as the object of improvement and comparison. The critical design variables of the cutter ring model are set to *T* values of 2, 3, 4, 5, 6, and 8. *A* values of 1, 2, 3, 4, and 5 mm. Table 1 presents the feature combination.

A simple naming rule is established: type + base size + number of changes (*T*) + range of changes (*A*). For example, VCS20T8A2 represents the VCS ring, with an outer diameter of 20 in, a blade width change amplitude of 2 mm, and a number of blade changes of 8. A similar CCS ring is named CCS20.

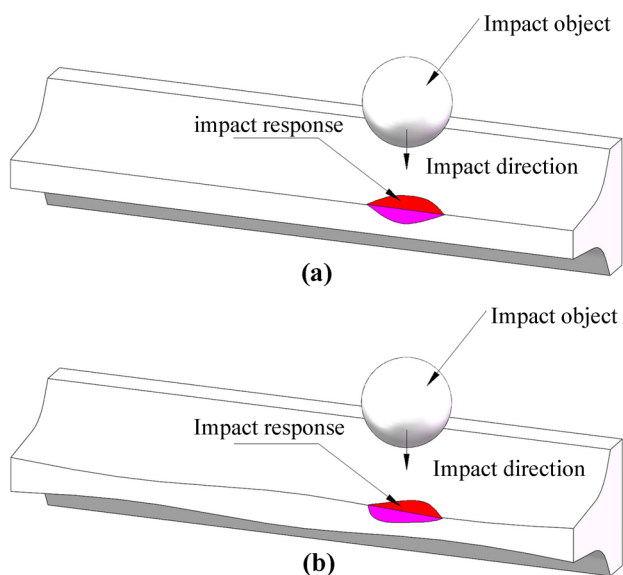


Fig. 10 Schematic of impact response of different types of cutter rings: **a** CCS type blade response to impact and **b** VCS type blade response to the impact

3 Simulation Modeling

3.1 Modeling and Validation Simulation of Rock

The purpose of this study is to use the FEM to simulate some performances of CCS and VCS disk cutters, and compare and analyze the data recorded in the simulation process, so as to get a summary with research value. Therefore, the establishment of an effective digital model is a necessary condition to ensure the accuracy of research results.

Table 2 Material properties of finite element Beishan granite model

Variables	Value	Unit
Density (ρ)	2600	kg/m ³
Elasticity modulus (E)	23.00	GPa
Poisson's ratio (μ)	0.23	
Tensile Strength (σ_t)	6.40	MPa
Uniaxial compressive strength (σ_c)	105.00	MPa

Table 1 Key variable feature combinations of 30 VCS cutter ring types

No	Feature	No	Feature	No	Feature	No	Feature	No	Feature
1	T2A1	7	T2A2	13	T2A3	19	T2A4	25	T2A5
2	T3A1	8	T3A2	14	T3A3	20	T3A4	26	T3A5
3	T4A1	9	T4A2	15	T4A3	21	T4A4	27	T4A5
4	T5A1	10	T5A2	16	T5A3	22	T5A4	28	T5A5
5	T6A1	11	T6A2	17	T6A3	23	T6A4	29	T6A5
6	T8A1	12	T8A2	18	T8A3	24	T8A4	30	T8A5

Granite is a common rock in mountain tunnel engineering. Compared with other types of rock, it has higher compressive strength and integrity, that's the way it is difficult to excavate. Therefore, granite is a commonly used material in the experimental study of the performance of tunnel-boring machine cutters. (Cho et al. 2010; Zhao et al. 2015).

Quite a few scholars have conducted experimental studies on the mechanical properties of Beishan granite, and obtained the mechanical properties of the rock by using UCS and BTS and other experimental methods, as shown in Table 2.

In this study, the influence of rock joint and other geological characteristics on the cutting effect is not considered, and the performance of disk cutters with different shapes in the homogeneous rock mass is merely compared. Therefore, it is assumed that the granite mass is isotropic solid with uniform and stable material. The 3D model of the granite sample was drawn in the software. The shape and size of the cylinder were 50 mm in diameter and 100 mm in altitude. The density, elasticity and plasticity characteristics of a material is defined in the material properties. The constitutive model of damage plasticity is preset in Abaqus software. The stress–strain and damage relationship of materials can be calculated and set as follows.

$$\sigma_t = \sigma_t(\epsilon_{tp}, \epsilon_{tr}) \tag{11}$$

$$\sigma_c = \sigma_c(\epsilon_{cp}, \epsilon_{cr}) \tag{12}$$

where the subscripts *t* and *c* refer to tension and compression, respectively; ϵ_{tp} and ϵ_{cp} are the equivalent plastic strains, ϵ_{tr} and ϵ_{cr} are the equivalent plastic strain rates.

When the rock specimen is unloaded from any point on the strain-softening branch of the stress–strain curves, the unloading response is weakened: the elastic stiffness of the material appears to be damaged (or degraded). The degradation of the elastic stiffness is characterized by two damage variables, d_t and d_c , which are assumed to be functions of the plastic strains:

$$d_t = d_t(\epsilon_{tp}); 0 \leq d_t \leq 1 \tag{13}$$

$$d_c = d_c(\epsilon_{cp}); 0 \leq d_c \leq 1 \tag{14}$$

The damage variables can take values from zero, representing the undamaged material, to one, which represents total loss of strength.

If E_0 is the initial (undamaged) elastic stiffness of the material, the stress–strain relations under uniaxial tension and compression loading are, respectively:

$$\sigma_t = (1 - d_t)E_0(\epsilon_t - \epsilon_{tp}) \tag{15}$$

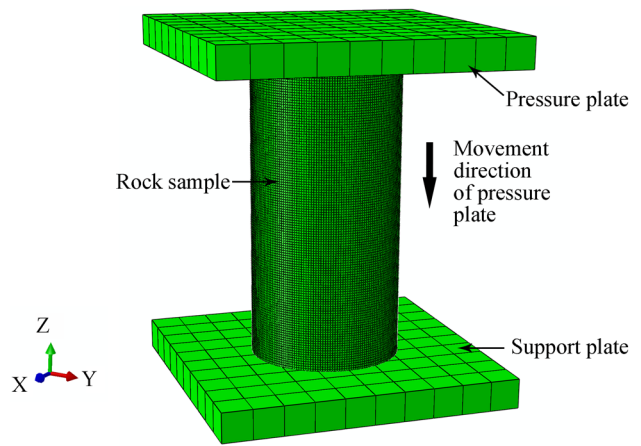


Fig. 11 Assembly diagram of UCS simulation experiment of rock

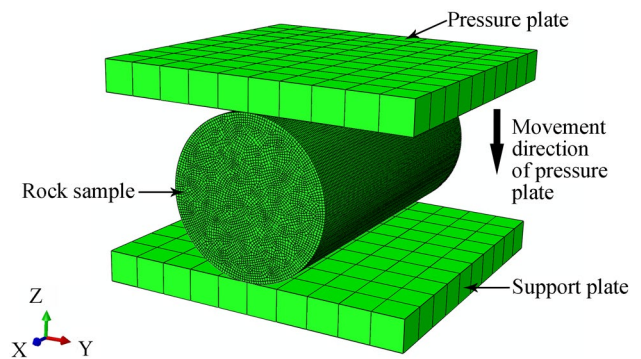


Fig. 12 Assembly diagram of BTS simulation experiment of rock

$$\sigma_c = (1 - d_c)E_0(\epsilon_c - \epsilon_{cp}) \tag{16}$$

Defined the “effective” tensile and compressive cohesion stresses as σ_{te} and σ_{ce} In the following functions.

$$\sigma_{te} = \frac{\sigma_t}{(1 - d_t)} = E_0(\epsilon_t - \epsilon_{tp}) \tag{17}$$

$$\sigma_{ce} = \frac{\sigma_c}{(1 - d_c)} = E_0(\epsilon_c - \epsilon_{cp}) \tag{18}$$

Design two identical cuboids, 100 mm* 100 mm* 10 mm in length, width and height, set as discrete rigid bodies, respectively, as support plates and pressure plates. The simulation assembly diagram of UCS and BTS is shown in Fig. 11 and Fig. 12.

In the load and boundary condition setting module of the two simulation models, the 6 degrees of freedom of the support plate are completely fixed, and the pressure plate can singly move uniformly along the opposite direction of the Z axis in a straight line with a speed of 1 mm/s. In UCS model,

the movement time of the pressure plate is set to 5 s, and in BTS model, the movement time of the pressure plate is set to 3 s. The rock sample is divided into hexahedron with a side length of 0.8 mm in the grid partition setting, and the support plate and the pressure plate are divided into hexahedron with a side length of 10 mm. After running the simulation, the stress–strain and damage data of the rock sample element can be read, and the accuracy of the elastic modulus, tensile strength and compressive strength of the model can be judged by comparing the experimental results.

In addition to the above three mechanical parameters, Poisson's ratio of rock samples is simulated. Using a method similar to the above, the rock sample model is set as a cuboid with a 5 mm side length, and the material is the same as the above simulation model. A rigid body pressure plate with a diameter of 10 mm is assembled on the upper surface of the rock model, and then the Z, Y, X three axes of the rock sample are fixed in the opposite direction. To keep the stress state of the rock at the elastic stage, set the pressure plate to uniformly move 0.01 mm/s along the opposite direction of Y axis, and set the movement time to 5 s. Then, the rock is divided into hexahedrons with 1 mm sides, as shown in Fig. 13. After running the simulation, the displacement data of three free surfaces of X, Y, Z can be read to calculate the Poisson's ratio of the rock model.

3.2 Modal Simulation

The CCS cutter ring model was established by referring to the size of the 20-inch disc cutter adopted in a section of the Jilin Project. The material of the cutter ring model was defined as die steel. The performance parameters and critical dimensions are presented in Table 3. The geometry of the VCS cutter rings is designed using the method described in the previous chapter.

Modal analysis was used to determine the natural frequencies of components. In replacing CCS cutter rings with VCS cutter rings, it is necessary to analyze natural frequency differences to ensure feasibility. The cutter ring model was

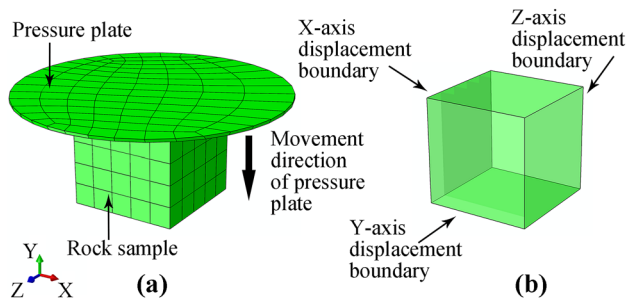


Fig. 13 Simulation of Poisson's ratio test of rock. a Assembly diagram. b Schematic diagram of boundary conditions

Table 3 Material properties of finite element cutter ring models

Variables	Value	Unit
Density (ρ)	7850	kg/m ³
Elasticity modulus (E)	210.00	GPa
Poisson's ratio (μ)	0.30	

imported into Abaqus, and the material was set as described above. In the analysis step, the linear perturbation analysis type was selected, the specific target frequency was selected, and 5 was selected for the number of steps. The inner diameter of the cutter ring was defined as the rotating sub-contract surface to simulate actual motion, and the cutter shoulders on both sides were defined as the limiting freedom surface. In the motion boundary condition, only one degree of freedom was opened—the rotation around the axis where the centerline is located—and the mesh size was set to 10 mm, as depicted in Fig. 14.

3.3 Impact Simulation

The impact model was established, and a ball with a diameter of 40 mm was used as the phantom impact object. The material was defined as metal, and the material performance was identical to that of the cutter ring.

Because of the complexity of the cutter ring operation environment, impact is the most common type of load encountered in the service process of the cutter ring. This experiment observes the difference between the impact responses of VCS and CCS cutter rings and analyzes the influence of two key design variables on the impact response. After importing the model of the cutter ring and impact material, the display dynamic analysis step

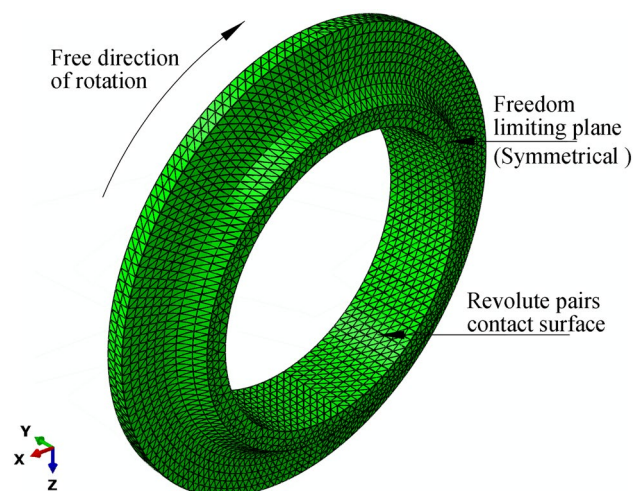


Fig. 14 Schematic of modal simulation modeling

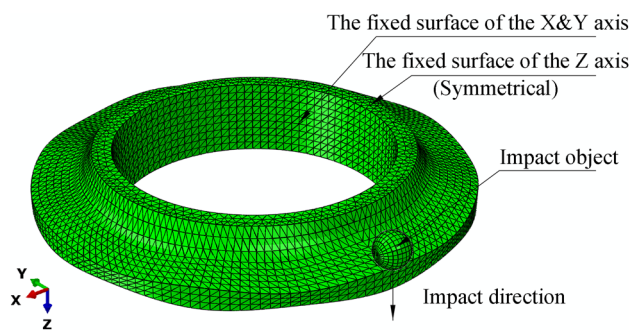


Fig. 15 Schematic of cutter ring impact simulation model



Fig. 16 Linear cutting experimental machine of Beijing University of Technology. (zhao et al. 2015)

was created, which lasted 0.05 s, and the process was 10 steps. The contact surface is defined as the impact surface (active) and the ring's blade side and blade face (passive).

The initial sports velocity of the impact object is set to 100 mm/s, and the movement is in the same Z-axis direction as the rotation axis of the cutter ring. The impact point is the highest and lowest point of the curve where the blade is located. The two sides of the cutter shoulder of the cutter ring were defined as the Z-axis limiting plane, and the inner diameter cylinder of the cutter ring was defined as the XY-axis limiting plane. The mesh size was set to 10 mm, as depicted in Fig. 15.

3.4 Rock-breaking Motion Simulation

This simulation model is designed according to the working principle of LCM, as shown in Fig. 16 is the full-size LCM of the University of Science and Technology Beijing. The

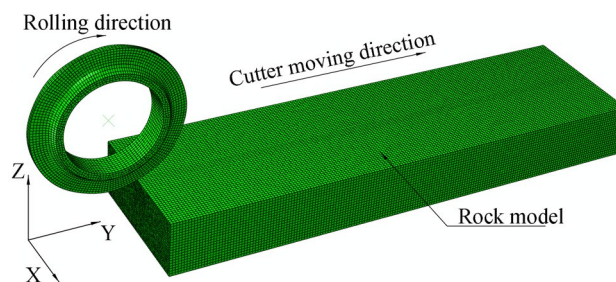


Fig. 17 Schematic of cutter ring rolling rock simulation model

purpose of the simulation is to observe the influence range of rock damage caused by the cutter rings with the same outer diameter and different blade shapes, and to analyze the influence of key design parameters of VCS cutter rings on the damage effect. Therefore, the cutter ring and rock should be pre-installed, as shown in Fig. 17, so that the radial symmetric plane of the cutter ring coincides with the center plane of the width of the rock, and the center of the cutter ring is 100 mm away from the edge of the rock in the Y direction.

The rock model was established based on the results of material property experiments of granite common in engineering as the previous chapter. The rock length was defined as 1800 mm, width as 500 mm, and thickness as 250 mm to ensure that the 20-in cutter ring roll was a complete circle on the rock model.

The projection interference is the distance between the cutter ring and the rock in the XZ plane; the penetration degree is 1.5 mm. The display dynamic analysis step is set, the motion time is set to 40 s, and the output course is set to 100 steps. When the boundary conditions of the cutter ring movement are set, only two degrees of freedom and boundary conditions of the cutter ring are opened, including the Y-axis movement speed of 50.8 mm/s and the rotation speed around the X-axis of 0.2 rad/s. The boundary conditions for the rock are established: the lower surface of the rock is fixed, the upper surface is a free surface, and the other four sides are symmetrical planes.

The contact surface type is set to face-to-face contact, the blade and the two sides of the blade are the active surfaces, and the upper surface of the rock is the passive surface. The cutter ring and the rock were divided into 10 mm grids. It is only necessary to replace the cutter rim model when conducting experiments on different cutter rims. The second cutter ring model was inserted during the secondary rolling experiment to adjust the relative pre-installed distance between the cutter ring and rock based on the requirements. The motion attributes and contact characteristics were identical to those of the first cutter ring.

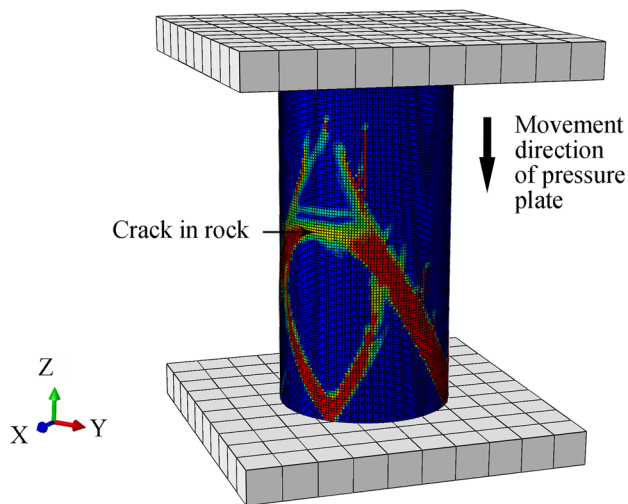


Fig. 18 Diagram of rock crack location in UCS simulation result

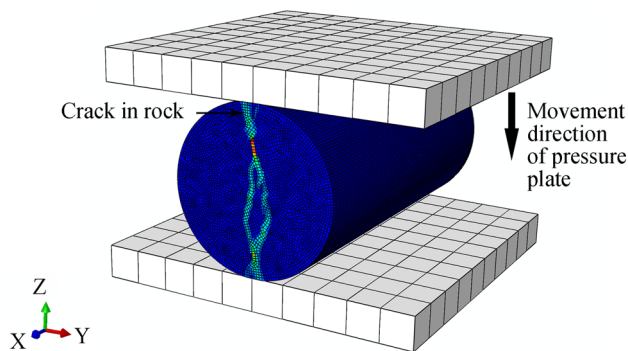


Fig. 19 Diagram of rock crack location in BTS simulation results

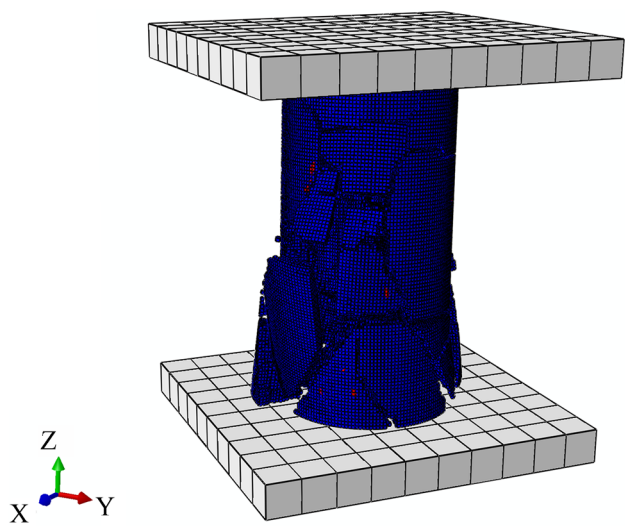


Fig. 20 Fracture result renderings correspond to Fig. 18

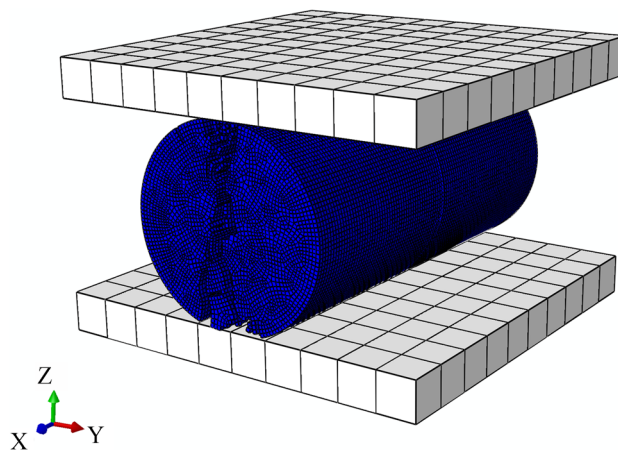


Fig. 21 Fracture result renderings correspond to Fig. 19

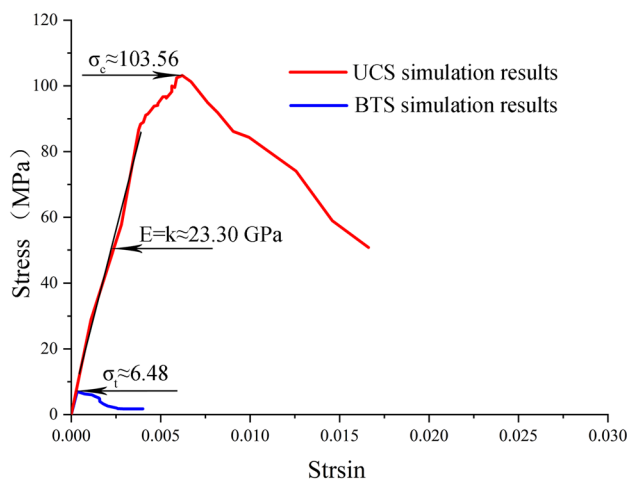


Fig. 22 Curve of stress–strain experimental data of UCS and BTS simulation

4 Experimental Simulation Results and Discussion

4.1 Verifying Simulation Results

Figures 18, 19, 20, 21 are the visualization results of UCS and BTS simulation. By reading the damage distribution of a rock model at a certain moment in the process of compression motion, the location of cracks can be intuitively seen, which is consistent with reality.

Read the data of the two simulation models in the process of motion, the average stress–strain curves of all elements of the rock sample are shown in Fig. 22. The slope of the fitted line segment in the elastic stage is 23.3019 GPa, the uniaxial compressive strength is 103.56 MPa and the tensile strength is 6.48 MPa.

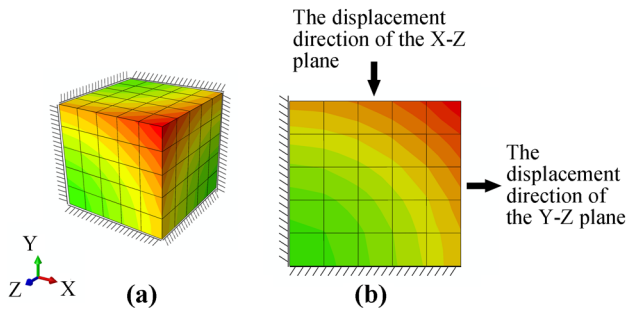


Fig. 23 Simulation test results of granite Poisson's ratio. **a** The cloud map of displacement distribution. **b** Direction of displacement

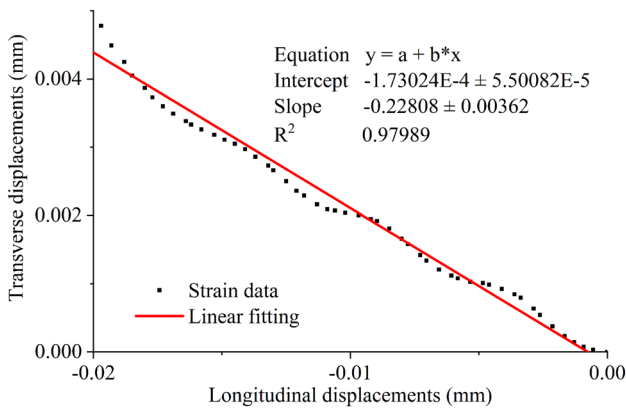


Fig. 24 Linear fitting diagram of transverse and longitudinal displacements

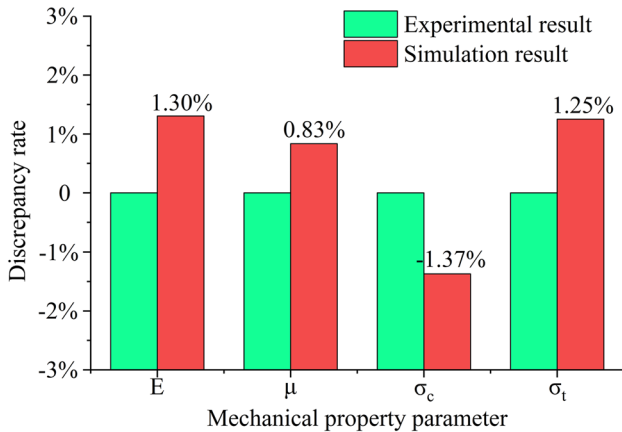


Fig. 25 The discrepancy rate of experimental and simulation mechanical properties of Beishan granite

The visualization results of Poisson's ratio simulation test are shown in Fig. 23, revealing the direction and size distribution of rock-free surface displacement. Figure 24 reveals the proportional relation of the surface displacement of the

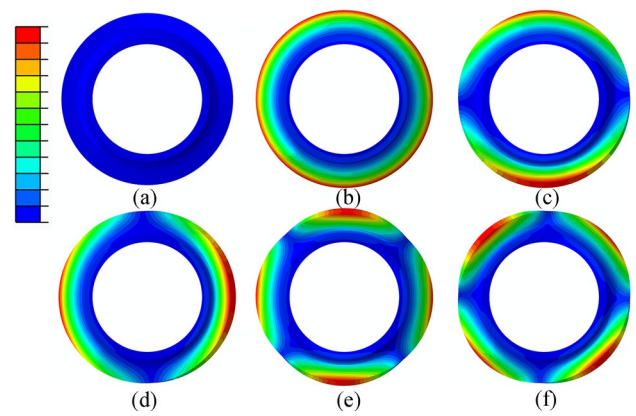


Fig. 26 Modal simulation results of cutter ring: **a** normal condition, **b** first mode vibration mode, **c** second mode vibration mode, **d** third mode vibration mode, **e** fourth mode vibration mode, and **f** fifth mode vibration mode

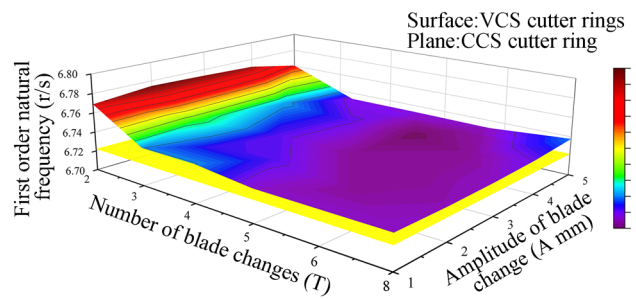


Fig. 27 3D diagram of first-order natural frequencies of each cutter ring

rock model. According to the slope of the fitted line segment and the definition of Poisson's ratio, it can be judged that Poisson's ratio of the rock model is 0.22808.

Figure 25 is the comparison consequence between the experiment and simulation of the mechanical properties of Beishan granite. As shown in the figure, the average discrepancy rate is very minor, about 1.19%, which proves the effectiveness of this rock model.

4.2 Modal Simulation Results

Modal simulation experiments of 30 types of VCS cutter rings and 1 type of CCS cutter ring arranged by two different variable parameters were conducted and produced similar results. The experimental results reveal the cutter ring's first five-order natural frequency values, modes of vibration, and amplitude range. The modes and amplitudes of 31 experimental results are similar, one of which is depicted in Fig. 26. The experimental results include the first five-order natural frequency values of each cutter ring and the speed values of resonance phenomena, all relatively high.

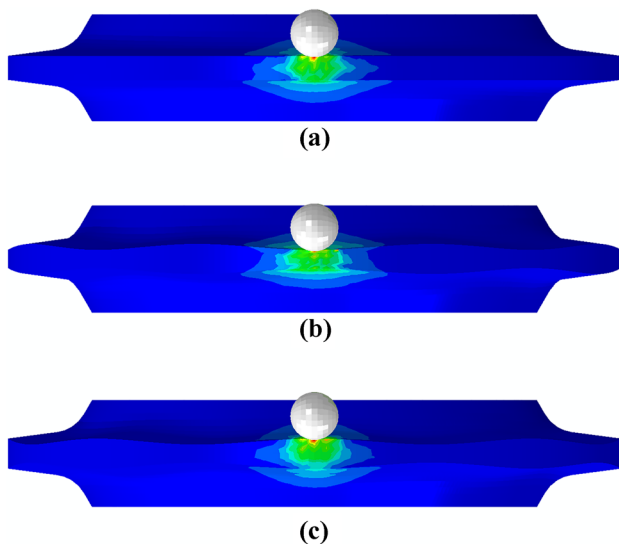


Fig. 28 The result of the impact on different positions of the cutter rings: **a** position of blade of CCS ring, **b** minimum section position of VCS cutter ring, and **c** maximum section position of VCS cutter ring

Therefore, only the first-order speed values of resonance of each cutter ring and their distribution rules are selected for analysis, as depicted in Fig. 27.

The results can be analyzed with the numerical distribution method. The VCS cutter circle of the first-order natural frequency is slightly higher than the cross-section cutter ring. Moreover, the greater the change in the VCS cutter circle T natural frequency, the closer it is to the cross-section cutter ring. The smaller the change in the A natural frequency, the closer it is to the cross-section cutter ring circle. The value of T and change in the impact on the natural frequency is A monotonous. Numerically, the first-order resonance occurs when the rotating speed is 6.72–6.78 rad/s. However, this is a very high rotating speed, which is impossible in real-world engineering, so the VCS cutter ring will not have resonance in practical applications.

4.3 Impact Simulation Results

Impact experiments were conducted at all blade positions of the CCS cutter ring and the maximum and minimum section blades of the 30 VCS cutter rings. The results are depicted in Fig. 28. Each cutter circle’s shock response is different. The strain energy is selected at a standard cutter stable level after the impact because the impact of stability of the attenuation value influences the cutter ring’s internal energy. The higher the architecture instability, the more impact-resistant and the lower the corresponding strain energy (Xue et al. 2018).

The impact response of any VCS cutter ring differs at different positions. The impact response of the same VCS

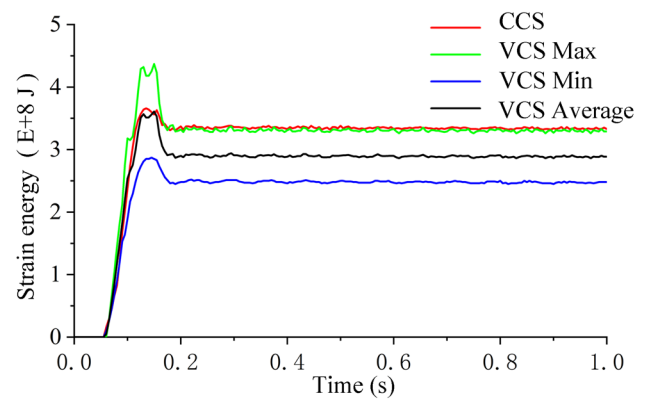


Fig. 29 Strain energy curves of the impact response of VCS and CCS cutter rings

moving ring at the maximum and minimum section positions is either higher or lower than the normal section. However, the impact-strain energy at the maximum section is higher than at the minimum section. The average values of the impact-strain energy of the maximum and minimum sections were compared with the strain energy of the CCS to analyze the results, as depicted in Fig. 29.

For the curve data depicted in Fig. 29, the average difference between the CCS curve and VCS average curve at each time point is the reference value for quantifying impact resistance, as defined in Eq. (14).

$$SE = \frac{1}{N} \sum_{i=1}^N \left(Y_i - \frac{Y_{1i} + Y_{2i}}{2} \right) \tag{19}$$

where SE is the quantified value of the cutter ring impact-strain energy, N is the sampling number of the strain energy curve, i is the number of sampling points on the strain energy curve, Y is the sampling value of the CCS cutter ring impact-strain energy curve, Y_1 is the sampling value of a VCS cutter ring maximum-section location impact-strain energy curve, and Y_2 is the sampling value of a VCS cutter ring minimum-section location impact-strain energy curve. The numerical value is transformed into Eq. (15) by mathematical normalization:

$$SE_k = \frac{SE_j}{\sum_{j=1}^{30} (SE_j)} \tag{20}$$

where SE_k is the normalized value of the impact-strain energy of the cutter ring, and j is the number of VCS cutter rings. A three-dimensional (3D) data chart based on the results is illustrated in Fig. 30. VCS20T6A4 has the highest impact resistance. The influence of the number of blade changes and the range of blade changes on the anti-impact

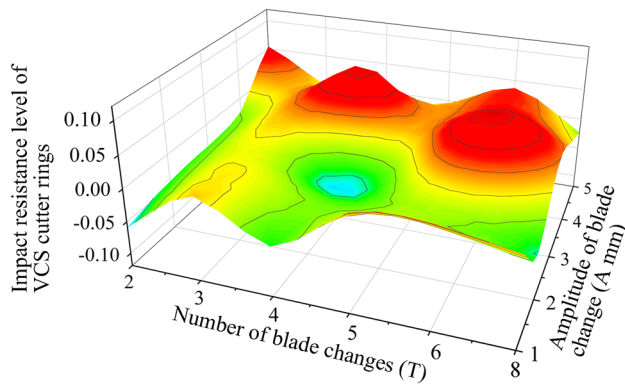


Fig. 30 3D diagram of impact resistance levels of VCS cutter rings

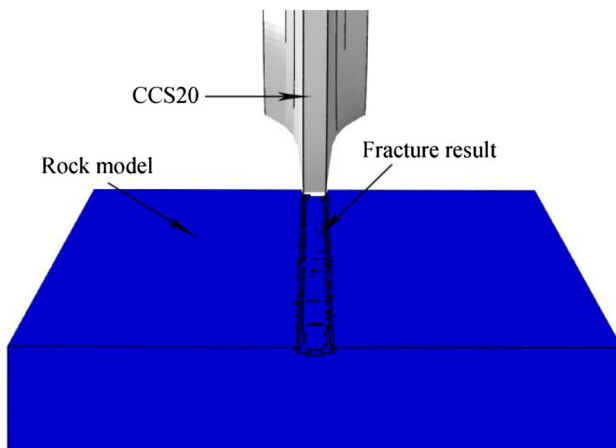


Fig. 31 Result of rock fracture caused by CCS20 cutter ring

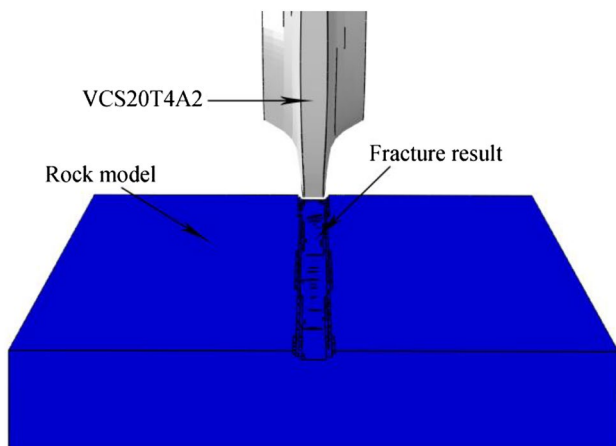


Fig. 32 Result of rock fracture caused by VCS20T4A2 cutter ring

performance of the VCS cutter ring is non-monotonous. Because it is challenging to summarize the rule, selecting a VCS cutter ring in engineering should be based on experimental data.

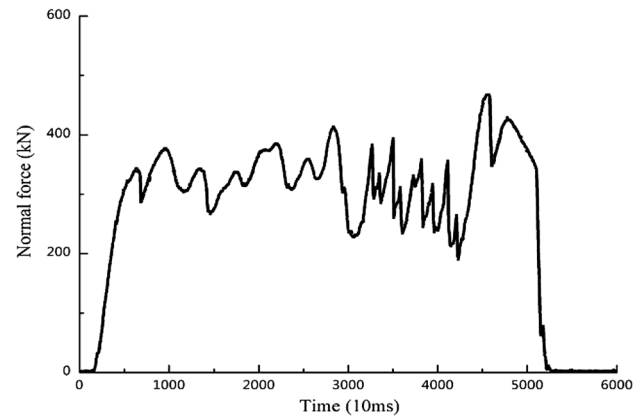


Fig. 33 Normal force change curve of LCM experiment. (zhao et al. 2015)

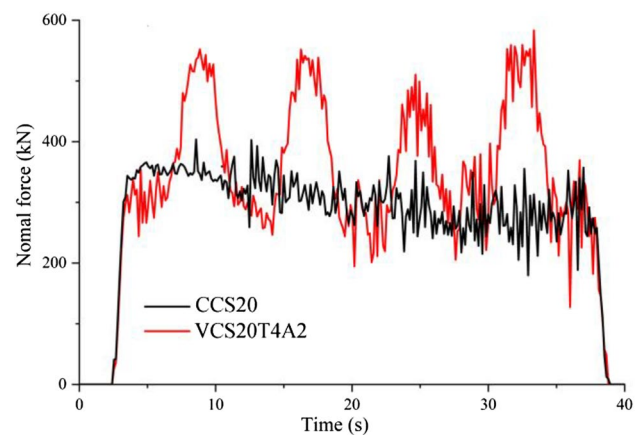


Fig. 34 Normal force change curve of LCM simulation by CCS and VCS disc cutter

4.4 Rock Failure Simulation Results

CCS cutter ring and 30 kinds of VCS cutter rings were simulated by LCM single cutting. Figures 31 and 32 show the results of rock fracture caused by CCS20 and VCS20T4A2 cutter ring, respectively. As shown in Fig. 33. Is the full-size LCM of the University of Science and Technology Beijing test result of normal force (zhao et al. 2015). The course curve of the CCS20 and VCS20T4A2 cutter rings subjected to the normal force in the process is shown in Fig. 34. And it is found that CCS cutting result is similar to the research of other scholars (Entacher et al. 2013). Therefore, it is judged that the simulation results are valid.

The stress distribution results of rock in the simulation process were read, and through comparison, it can be seen that the number of blade changes T has a significant influence on the distribution shape of the stress nephogram, as shown in Fig. 35. VCS cutting ring has a wider stress range

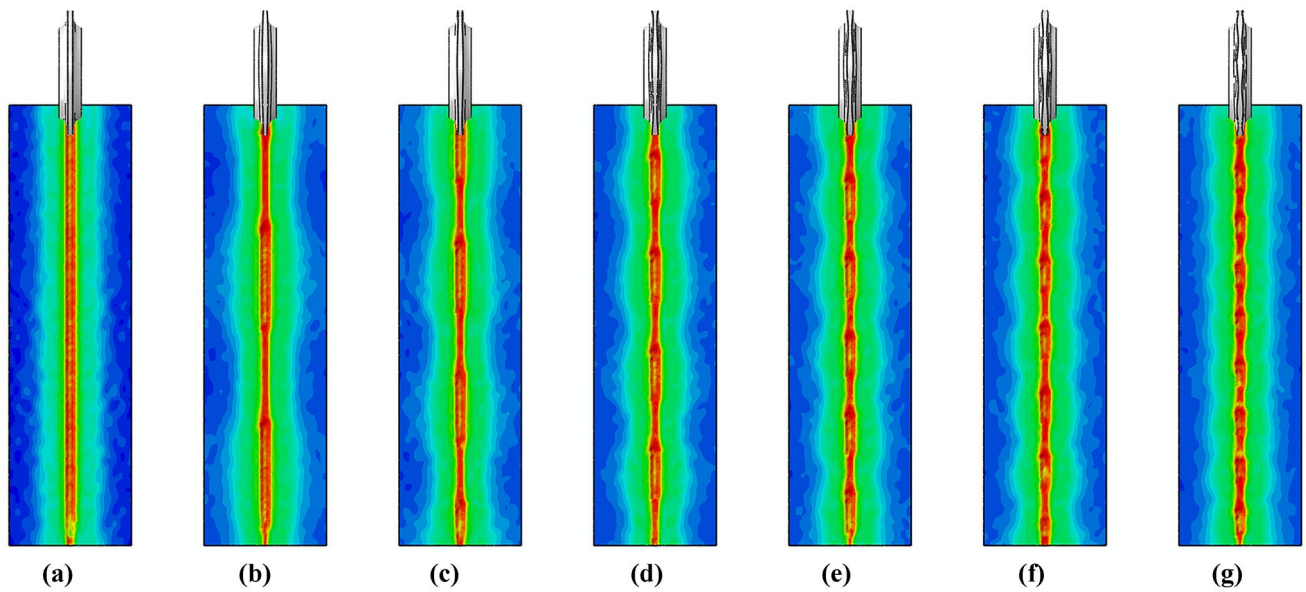


Fig. 35 When the design variable A is the same and T is different, the rock failure results of a VCS cutter ring and CCS cutter ring are compared: a CCS20, b VCS20T2A5, c VCS20T3A5, d VCS20T4A5, e VCS20T5A5, f VCS20T6A5, and g VCS20T8A5

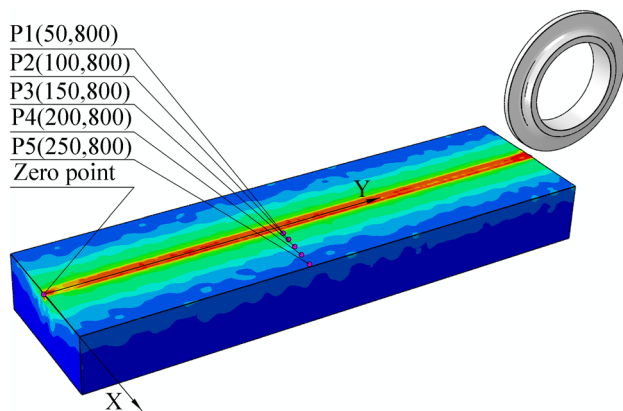


Fig. 36 In the visual model of experimental results, five elements were selected to conduct the schematic of stress analysis

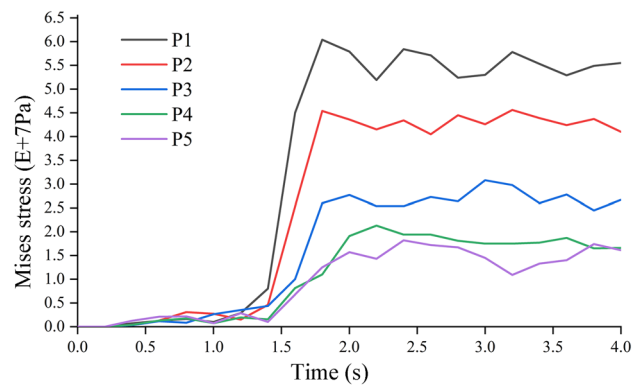


Fig. 37 Stress-time curves at five selected points

on rock than CCS cutting ring, and the damage effect is ideal.

However, if the influence of variation amplitude A on the distribution of the stress cloud map is reflected in the width of the isosurface, the difference is relatively small and difficult to observe. A quantitative method is necessary to compare the failure effect. Thus, several elements are selected from the finite element model of experimental results to observe the history curve of their stress changes with time. Five elements were selected for stress data extraction at 800 mm from the initial edge of rolling and 50 mm from the center of rolling, as depicted in Fig. 36, to study the failure range.

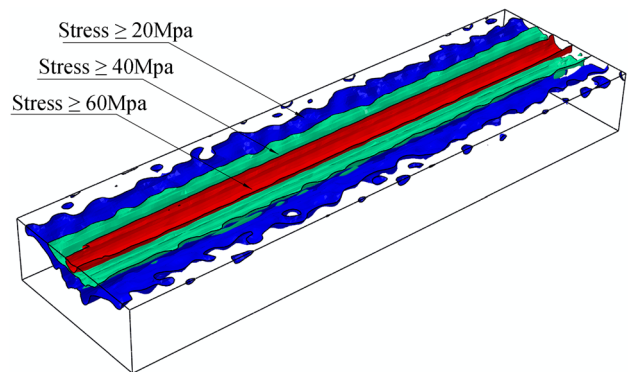


Fig. 38 Schematic of stress contour surface in visual experimental results

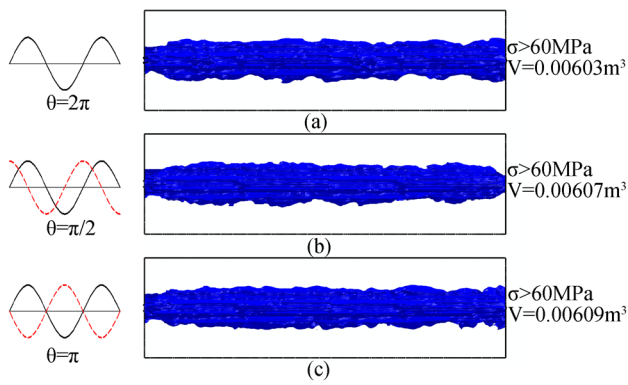


Fig. 39 Schematic of influence of different phase angles on failure effect in simulation experiment results of rock rolling twice with VCST2A2 cutter ring: **a** when $\theta=2\pi$, the volume of rock damage V is 0.00603m^3 , **b** when $\theta=\pi/2$, the volume of rock damage V is 0.00607m^3 , and **c** when $\theta=\pi$, the volume of rock damage V is 0.00609m^3 .

The corresponding stress curves are depicted in Fig. 37. The closer the rock element is to the rolling center, the greater the stress. The rock model was then divided into stress equivalents of 20, 40, and 60 MPa, as depicted in Fig. 38. The yield strength of the rock model is 60 Mpa, so the area where the stress is greater than 60 Mpa should have started to break. Consequently, measuring the rock volume value of the isosurface envelope of 60 Mpa can be used as the standard to measure the rock failure effect.

In engineering practice, the disc cutter should be repeatedly rolled on the same track, so it must simulate the

rolling many times. For the CCS cutter ring, the rolling track is coincident. For the VCS cutter ring, the trajectory of rolling two times is almost not coincident, resulting in a phase angle.

The influence of the phase angle of the VCS cutter ring on the failure effect when the cutter ring is rolled twice was observed and compared. With the VCST2A5 cutter ring as an example, comparative experiments were conducted under the three conditions of phase angles 2π , $\pi/2$, and π . The results, depicted in Fig. 39, demonstrate that the failure effect is the smallest when the overlapping phase angle of the rock track is 2π ; the same results can be obtained using other VCS cutter ring models.

The phase angle for two PI two rolling simulation experiments was used to compare the two key design variables for the effects of the VCS cutter broken rock circle with the minimum damage method. As depicted in Fig. 40, when the extracted rocky body of the stress is greater than 60 MPa for data analysis, the destructive effect of the VCS cutter ring is often less severe than the section cutter ring.

The statistics on the volume data of rock broken by cutter rings are calculated as follows to quantitatively compare the rock-breaking capacity differences between different VCS and CCS cutter rings:

$$VO = Y_{li} - \frac{1}{30} \sum_{i=1}^{30} (Y_{li} - Y) \quad (21)$$

where VO is the quantified value of the cutter ring failure volume, Y_1 is the volume of rock damaged by the VCS

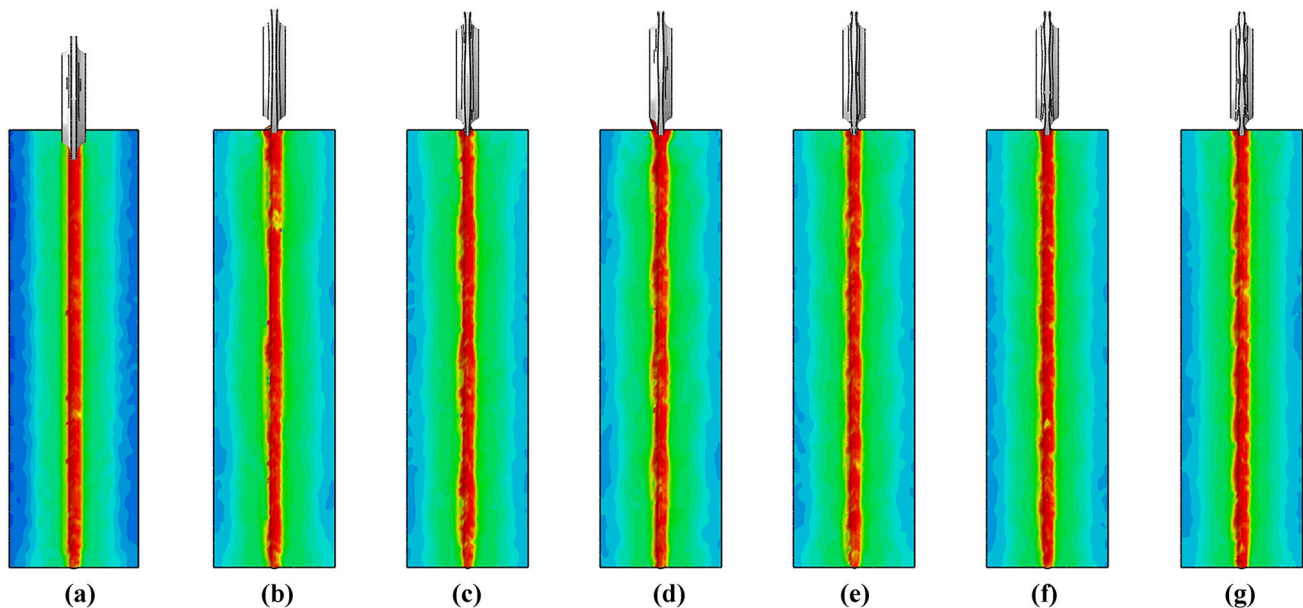


Fig. 40 When rolling twice and the design variables A are the same and T are different, the rock failure results of a VCS cutter ring and equal section cutter ring are compared: **a** CCS20, **b** VCS20T2A5, **c** VCS20T3A5, **d** VCS20T4A5, **e** VCS20T5T5, **f** VCS20T6A5, and **g** VCS20T8A5

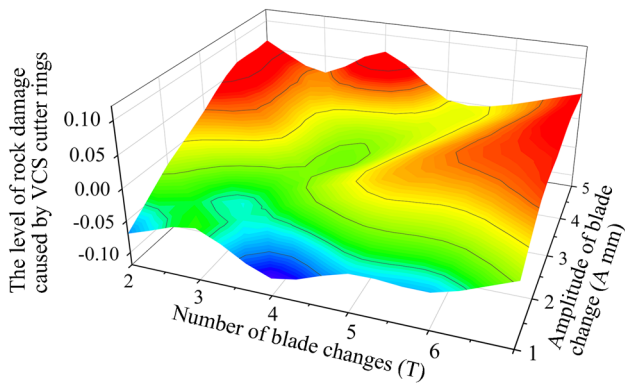


Fig. 41 3D diagram of rock damage levels caused by VCS cutter rings

cutter ring, Y is the volume of rock damaged by the CCS cutter ring, and I is the number of VCS cutter rings. The numerical value is transformed into the following by mathematical normalization:

$$VO_k = \frac{VO_i}{\sum_{i=1}^{30}(VO_i)} \quad (22)$$

In Eq. (15), VO_k is the normalized value of the damaged volume of the cutter ring, where I is the number of VCS cutter rings. A 3D data chart based on the results is illustrated in Fig. 41, demonstrating that VCST2A5 has a remarkably high rock-breaking effect.

4.5 Discussion

There were four initial assumptions when designing this program. The FEM analysis results confirmed the authenticity and feasibility of each assumption.

First, the VCS cutter ring replaces the CCS cutter ring with the same outer diameter size. Based on the modal analysis results, applying a VCS cutter ring designed using the design method mentioned in the text and variable value will not cause resonance in the project. Therefore, the replacement behavior of the cutter ring is feasible. Furthermore, because the design method of a VCS cutter ring is not unique, the design method of a VCS cutter ring with other variable design methods may cause changes in the vibration field.

The second is the impact resistance of the VCS cutter ring. Based on the impact simulation experiment results, the impact resistance of some VCS rings is higher than the CCS ring, while those of others are lower. However, the impact in real-world engineering is much more

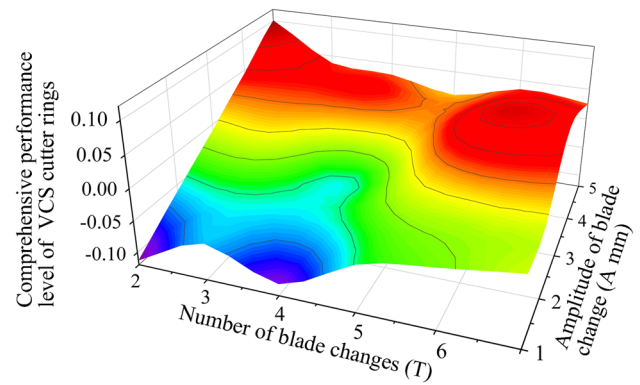


Fig. 42 3D diagram of the comprehensive performance level of VCS cutter rings

complicated than in the experiment, with more in-depth research on the impact resistance.

Third, the rock-breaking effect of a VCS cutter ring is confirmed to be ideal. The stress range of rock generated by the VCS cutter ring is broader than the CCS cutter ring for both single rolling and multiple rolling. The wear rate is not considered because the friction rate strongly correlates with the pressure contact area. The blade area of the VCS ring in this study is the same as that of the existing CCS ring, so the pressure contact area is also relatively close. The experimental method of wear and work correlation will be studied in future research.

Fourth, given the performance of the VCS cutter ring, the final statistical results of the above impact resistance test and rock rolling test are superior, and the results can again be obtained by normalization statistics. As depicted in Fig. 42, both VCST6A4 and VCST2A5 have adequate comprehensive effects, among which VCST6A4 has outstanding impact resistance and is suitable for rocks with relatively developed joints and complex structures. VCST2A5 has a remarkably high rock-breaking effect and is suitable for rock bodies with relatively single, stable structures and high integrity.

5 Conclusions

In this paper, a variable cross-section (VCS) cutter ring is designed, and several simulations and comparative experiments are conducted using the FEM. Finally, a VSC cutter ring that can adapt to granite with uniaxial compressive strength of 105 MPa, a tensile strength of 6.4 MPa is obtained. The change period of the VCS cutter ring is 2, and the change range is 5 mm.

First, according to the rock-breaking principle of the cutter ring, the failure form of the cutter ring, and the mechanical characteristics of the rock, the parametric design method

of the VCS cutter ring is established based on the traditional CCS cutter ring, and 30 digital models of the 20-in VCS cutter ring are established using the change period and change amplitude as parameters.

Secondly, the FEM is used to model the rock and the UCS, BTS and Poisson's ratio test simulation are carried out. By comparing the actual experimental results with the simulation results, it is known that the average discrepancy rate of the elastic modulus, Poisson's ratio, uniaxial compressive strength and tensile strength is 1.19%, which verifies the effectiveness of the simulation model of rock samples.

Third, the modal simulation experiment is conducted, and the natural vibration frequencies of VCS and CCS cutter rings are obtained—both are very close to 6.72 rad/s, verifying the feasibility of interchangeability between them.

Fourth, the impact simulation of 30 types of VCS cutter rings and the simulation of rolling on the rock are conducted, and the simulation results of CCS cutter rings are compared with those of CCS cutter rings. The results demonstrate that most VCS cutter rings have higher impact resistance than CCS cutter rings, and VCS cutter rings have a higher damage effect on rock than CCS cutter rings.

Fifth, the impact resistance performance of the 30 VCS cutter rings and the performance of the damaged rock were ranked using a statistical analysis method with 3D data. After mathematical normalization, the two data groups were superimposed to obtain the optimal design parameters.

The experimental results confirmed that the VCS cutter ring has some advantages over the CCS cutter ring. However, several factors have not been considered, such as wear properties, thermal impact properties, the influence of dynamic parameters on the performance, and cutting tool system layout impact on performance. Future research will consider these factors.

Funding Industrial Technology Research and Development of Jilin Province, 2021C038-4, Xian Yong Zhu, Scientific research project of Jilin Provincial Department of education in 2021, JJKH20211078KJ, Song Yang.

Data availability The computational data used in this study will be made available on request.

References

- Balci C, Tumac D (2012) Investigation into the effects of different rocks on rock cuttability by a V-type disc cutter. *Tunn Undergr Space Technol* 30:183–193. <https://doi.org/10.1016/j.tust.2012.02.018>
- Barzegari G, Uromeihy A, Zhao J (2015) Parametric study of soil abrasivity for predicting wear issue in TBM tunneling projects. *Tunn Undergr Space Technol* 48:43–57. <https://doi.org/10.1016/j.tust.2014.10.010>
- Cardu M, Iabichino G, Oreste P, Rispoli A (2016) Experimental and analytical studies of the parameters influencing the action of TBM disc tools in tunnelling. *Acta Geotech* 12:293–304. <https://doi.org/10.1007/s11440-016-0453-9>
- Chang SH, Choi SW, Bae GJ, Jeon S (2006) Performance prediction of TBM disc cutting on granitic rock by the linear cutting test. *Tunnel Undergr Space Tech*. <https://doi.org/10.1016/j.tust.2005.12.131>
- Cho JW, Jeon S, Yu SH, Chang SH (2010) Optimum spacing of TBM disc cutters: a numerical simulation using the three-dimensional dynamic fracturing method. *Tunn Undergr Space Technol* 25:230–244. <https://doi.org/10.1016/j.tust.2009.11.007>
- Choi SO, Lee SJ (2014) Three-dimensional numerical analysis of the rock-cutting behavior of a disc cutter using particle flow code. *KSCE J Civ Eng* 19:1129–1138. <https://doi.org/10.1007/s12205-013-0622-4>
- Entacher M, Winter G, Galler R (2013) Cutter force measurement on tunnel boring machines – Implementation at Koralm tunnel. *Tunn Undergr Space Technol* 38:487–496. <https://doi.org/10.1016/j.tust.2013.08.010>
- Geng Q, Wei Z, Meng H, Macias FJ, Bruland A (2016) Free-face-assisted rock breaking method based on the multi-stage tunnel boring machine (TBM) Cutterhead. *Rock Mech Rock Eng* 49:4459–4472. <https://doi.org/10.1007/s00603-016-1053-6>
- Geng Q, Bruland A, Macias FJ (2017) Analysis on the Relationship between layout and consumption of face cutters on hard rock tunnel boring machines (TBMs). *Rock Mech Rock Eng* 51:279–297. <https://doi.org/10.1007/s00603-017-1320-1>
- Gertsch R, Gertsch L, Rostami J (2007) Disc cutting tests in colorado red granite: implications for TBM performance prediction. *Int J Rock Mech Min Sci* 44:238–246. <https://doi.org/10.1016/j.ijrmm.2006.07.007>
- Gong QM, Jiao YY, Zhao J (2006) Numerical modelling of the effects of joint spacing on rock fragmentation by TBM cutters. *Tunn Undergr Space Technol* 21:46–55. <https://doi.org/10.1016/j.tust.2005.06.004>
- Gong Q, Yin L, Ma H, Zhao J (2016) TBM tunnelling under adverse geological conditions: An overview. *Tunn Undergr Space Technol* 57:4–17. <https://doi.org/10.1016/j.tust.2016.04.002>
- Hassanpour J (2018) Development of an empirical model to estimate disc cutter wear for sedimentary and low to medium grade metamorphic rocks. *Tunn Undergr Space Technol* 75:90–99. <https://doi.org/10.1016/j.tust.2018.02.009>
- Herrenknecht., MRS, L., Maidl. (2008). *Hardrock Tunnel Boring Machines*. 343 pp. <https://doi.org/10.1002/9783433600122>
- Huo J, Sun W, Chen J, Zhang X (2011) Disc cutters plane layout design of the full-face rock tunnel boring machine (TBM) based on different layout patterns. *Comput Ind Eng* 61:1209–1225. <https://doi.org/10.1016/j.cie.2011.07.011>
- Li XF, Li HB, Liu YQ, Zhou QC, Xia X (2016) Numerical simulation of rock fragmentation mechanisms subject to wedge penetration for TBMs. *Tunn Undergr Space Technol* 53:96–108. <https://doi.org/10.1016/j.tust.2015.12.010>
- Li X, Feng F, Li D (2018) Numerical simulation of rock failure under static and dynamic loading by splitting test of circular ring. *Eng Fract Mech* 188:184–201. <https://doi.org/10.1016/j.engfractmech.2017.08.022>
- Lin L, Mao Q, Xia Y, Zhu Z, Yang D, Guo B, Lan H (2017) Experimental study of specific matching characteristics of tunnel boring machine cutter ring properties and rock. *Wear* 378–379:1–10. <https://doi.org/10.1016/j.wear.2017.01.072>
- Liu J, Cao P (2015) Study on rock fracture with tbn cutter under different confining stresses. *Indian Geotech J* 46:104–114. <https://doi.org/10.1007/s40098-015-0148-4>
- Liu J, Cao P, Han D (2015a) Sequential indentation tests to investigate the influence of confining stress on rock breakage by tunnel

- boring machine cutter in a biaxial state. *Rock Mech Rock Eng* 49:1479–1495. <https://doi.org/10.1007/s00603-015-0843-6>
- Liu J, Cao P, Li K (2015b) A study on isotropic rock breaking with TBM cutters under different confining stresses. *Geotech Geol Eng* 33:1379–1394. <https://doi.org/10.1007/s10706-015-9907-3>
- Liu J, Cao P, Han D (2016a) The influence of confining stress on optimum spacing of TBM cutters for cutting granite. *Int J Rock Mech Min Sci* 88:165–174. <https://doi.org/10.1016/j.ijrmms.2016.07.017>
- Liu Q, Huang X, Gong Q, Du L, Pan Y, Liu J (2016b) Application and development of hard rock TBM and its prospect in China. *Tunn Undergr Space Technol* 57:33–46. <https://doi.org/10.1016/j.tust.2016.01.034>
- Liu Q, Liu J, Pan Y, Zhang X, Peng X, Gong Q, Du L (2017) A wear rule and cutter life prediction model of a 20-in. TBM cutter for granite: a case study of a water conveyance tunnel in china. *Rock Mech Rock Eng* 50:1303–1320. <https://doi.org/10.1007/s00603-017-1176-4>
- Mirahmadi M, Tabaei M, Dehkordi MS (2017) Estimation of the specific energy of TBM using the strain energy of rock mass, case study: amir-kabir water transferring tunnel of Iran. *Geotech Geol Eng* 35:1991–2002. <https://doi.org/10.1007/s10706-017-0222-z>
- Moon T, Oh J (2011) A study of optimal rock-cutting conditions for hard rock TBM using the discrete element method. *Rock Mech Rock Eng*. <https://doi.org/10.1007/s00603-011-0180-3>
- Pan Y, Liu Q, Liu J, Peng X, Kong X (2018) Full-scale linear cutting tests in chongqing sandstone to study the influence of confining stress on Rock Cutting Forces by TBM disc cutter. *Rock Mech Rock Eng* 51:1697–1713. <https://doi.org/10.1007/s00603-018-1412-6>
- Park JY, Kang H, Lee JW, Kim JH, Oh JY, Cho JW, Rostami J, Kim HD (2018) A study on rock cutting efficiency and structural stability of a point attack pick cutter by lab-scale linear cutting machine testing and finite element analysis. *Int J Rock Mech Min Sci* 103:215–229. <https://doi.org/10.1016/j.ijrmms.2018.01.034>
- Plinninger R, Käsling H, Thuro K, Spaun G (2003) Testing conditions and geomechanical properties influencing the CERCHAR abrasiveness index (CAI) value. *Int J Rock Mech Min Sci* 40:259–263. [https://doi.org/10.1016/s1365-1609\(02\)00140-5](https://doi.org/10.1016/s1365-1609(02)00140-5)
- Qi G, Zheng YW, Hao M (2016) An experimental research on the rock cutting process of the gage cutters for rock tunnel boring machine (TBM). *Tunn Undergr Space Technol* 52:182–191. <https://doi.org/10.1016/j.tust.2015.12.008>
- Rostami J (2013) Study of pressure distribution within the crushed zone in the contact area between rock and disc cutters. *Int J Rock Mech Min Sci* 57:172–186. <https://doi.org/10.1016/j.ijrmms.2012.07.031>
- Tan Q, Yi L, Xia YM (2018) Performance prediction of TBM disc cutting on marble rock under different load cases. *KSCE J Civ Eng* 22:1466–1472. <https://doi.org/10.1007/s12205-017-1048-1>
- Tumac D, Balci C (2015) Investigations into the cutting characteristics of CCS type disc cutters and the comparison between experimental, theoretical and empirical force estimations. *Tunn Undergr Space Technol* 45:84–98. <https://doi.org/10.1016/j.tust.2014.09.009>
- Wang L, Kang Y, Cai Z, Zhang Q, Zhao Y, Zhao H, Su P (2012) The energy method to predict disc cutter wear extent for hard rock TBMs. *Tunn Undergr Space Technol* 28:183–191. <https://doi.org/10.1016/j.tust.2011.11.001>
- Wang L, Li H, Zhao X, Zhang Q (2017) Development of a prediction model for the wear evolution of disc cutters on rock TBM cutterhead. *Tunn Undergr Space Technol* 67:147–157. <https://doi.org/10.1016/j.tust.2017.05.003>
- Xia YM, Guo B, Cong GQ, Zhang XH, Zeng GY (2017) Numerical simulation of rock fragmentation induced by a single TBM disc cutter close to a side free surface. *Int J Rock Mech Min Sci* 91:40–48. <https://doi.org/10.1016/j.ijrmms.2016.11.004>
- Xia YM, Guo B, Tan Q, Zhang XH, Lan H, Ji ZY (2018) Comparisons between experimental and semi-theoretical cutting forces of CCS disc cutters. *Rock Mech Rock Eng* 51:1583–1597. <https://doi.org/10.1007/s00603-018-1400-x>
- Xiao N, Zhou XP, Gong QM (2017) The modelling of rock breakage process by TBM rolling cutters using 3D FEM-SPH coupled method. *Tunn Undergr Space Technol* 61:90–103. <https://doi.org/10.1016/j.tust.2016.10.004>
- Xue YD, Zhao F, Zhao HX, Li X, Diao ZX (2018) A new method for selecting hard rock TBM tunnelling parameters using optimum energy: a case study. *Tunn Undergr Space Technol* 78:64–75. <https://doi.org/10.1016/j.tust.2018.03.030>
- Yang H, Wang H, Zhou X (2015) Analysis on the Rock-Cutter interaction mechanism during the tbm tunneling process. *Rock Mech Rock Eng* 49:1073–1090. <https://doi.org/10.1007/s00603-015-0796-9>
- Zhao XB, Yao XH, Gong QM, Ma HS, Li XZ (2015) Comparison study on rock crack pattern under a single normal and inclined disc cutter by linear cutting experiments. *Tunn Undergr Space Technol* 50:479–489. <https://doi.org/10.1016/j.tust.2015.09.002>
- Zhao JL, Zhu XY, Hou ZH, Liu C, Yang S, Xiao X (2022) Design and finite element analysis of a variable cross-section cutter ring. *Simul Model Practice Theory*. <https://doi.org/10.1016/j.simpat.2021.102423>

Publisher's Note Springer Nature remains neutral with regard to jurisdictional claims in published maps and institutional affiliations.

Springer Nature or its licensor (e.g. a society or other partner) holds exclusive rights to this article under a publishing agreement with the author(s) or other rightsholder(s); author self-archiving of the accepted manuscript version of this article is solely governed by the terms of such publishing agreement and applicable law.